

A MULTI-WAVELENGTH STUDY OF PSR J1119–6127 AFTER 2016 OUTBURST

H.-H. WANG¹, L.C.-C. LIN², S. DAI³, J. TAKATA¹, K.L. LI², C.-P. HU^{4,†}, X. HOU^{5,6}

Draft version September 3, 2020

ABSTRACT

PSR J1119–6127, a high-magnetic field pulsar detected from radio to high-energy wavelengths, underwent a magnetar-like outburst beginning on July 27, 2016. In this paper, we study the post-outburst multi-wavelength properties of this pulsar from the radio to GeV bands and discuss its similarity with the outburst of the magnetar XTE J1810–197. In phase-resolved spectral analysis of 0.5–10 keV X-ray data collected in August 2016, the on-pulse and off-pulse spectra are both characterized by two blackbody components and also require a power-law component similar to the hard X-ray spectra of magnetars. This power-law component is no longer distinguishable in data from December, 2016. We likewise find that there was no substantial shift between the radio and X-ray pulse peaks after the 2016 X-ray outburst. The gamma-ray pulsation after the X-ray outburst is confirmed with data taken after 2016 December and the pulse structure and phase difference between the gamma-ray and radio peaks (~ 0.4 cycle) are also consistent with those before the X-ray outburst. These multi-wavelength observations suggest that the re-configuration of the global magnetosphere after 2016 magnetar-like outburst at most continued for about six months. We discuss the evolution of the X-ray emission after the 2016 outburst with the untwisting magnetosphere model.

1. INTRODUCTION

An isolated pulsar is a rapidly rotating and highly-magnetized neutron star with a spin period of ~ 1 ms– ~ 10 s and a surface dipole field of $B_s \sim 10^{8-15}$ G. Magnetars form a subclass of pulsars with bright and variable emission in the X-ray and gamma-ray band (Kaspi & Beloborodov 2017). Since the observed radiation from the magnetars exceeds the spin-down power of the pulsar, it has been suggested that decay of an ultra-high magnetic field that exceeds the critical magnetic field of $B_c = m_e^2 c^3 / e \hbar \sim 4.4 \times 10^{13}$ G provides the energy source of the emission (Thompson & Duncan 1996). The most remarkable feature of magnetars is their short, bright bursts, likely powered by a sudden release of energy from the star’s magnetic field (Woods & Thompson 2006; Ng et al. 2011; Pons & Rea 2012). Some bursts are accompanied by longer duration outburst states. It has been confirmed that some rotation powered pulsars (RPPs) with a high magnetic field strength ($B_s > 10^{13}$ G, hereafter high- B pulsars) also show magnetar-like X-ray outbursts (Livingstone et al. 2010; Archibald et al. 2016), and these high- B pulsars could provide a connection between magnetars and the usual RPPs.

Observed X-ray outbursts of magnetars are frequently accompanied by a glitch. Glitches are a sudden change in the spin frequency (f) and spin-down rate (\dot{f}), and

the radio observations have revealed ~ 180 glitching pulsars (Espinoza et al. 2011). The distribution is bimodal in glitch size ($\Delta f/f$) and is divided into large (small) glitches with $\Delta f/f \geq 10^{-7}$ ($\leq 10^{-7}$). Magnetar glitches are large (Dib et al. 2008), and the main difference with respect to glitches of normal pulsars is the presence of an accompanying X-ray outburst and pulse shape change (Kaspi et al. 2003; Woods et al. 2004), typically absent for glitches of normal pulsars.

PSR J1119–6127 is a high- B pulsar with an inferred polar strength of $B_s \sim 6.4 \times 10^{19} \sqrt{P\dot{P}} = 8 \times 10^{13}$ G (Camilo et al. 2000), with a spin period $P = 0.407$ s and a period time derivative $\dot{P} = 4 \times 10^{-12} \text{ s s}^{-1}$, giving a characteristic age and spin-down power of the pulsar $\tau_c = P/2\dot{P} = 1.6$ kyr and $\dot{E}_{sd} = 2.3 \times 10^{36} \text{ erg s}^{-1}$, respectively. This pulsar was discovered in the Parkes multibeam pulsar survey (Camilo et al. 2000) and it is likely associated with the supernova remnant G292.2-0.5 (Crawford et al. 2001) at a distance of 8.4 kpc (Caswell et al. 2004). Pulsed emission was also detected in the X-ray and gamma-ray bands (Gonzalez & Safi-Harb 2003; Parent et al. 2011). PSR J1119–6127 glitched in 1999, 2004, and 2007 (Camilo et al. 2000; Weltevrede et al. 2011a; Antonopoulou et al. 2015). The glitches of 2004 and 2007 exhibited a recovery of the spin-down rate toward the pre-glitch level, but that of 2007 showed an over-recovery that continued to evolve on a time scale of years (Antonopoulou et al. 2015). Unusually, the 2007 glitch was also accompanied by an X-ray outburst, with a temporary change in the radio pulse profile from single- to double-peaked (Weltevrede et al. 2011a).

The *Fermi* Gamma-ray Burst Monitor (GBM) and *Swift* Burst Alert Telescope (BAT) both triggered on magnetar-like X-ray outbursts of PSR J1119–6127 on 2016 July 27 UT 13:02:08 (Younes et al. 2016) and on 2016 July 28 UT 01:27:51 (Kennea et al. 2016). Göğüş et al. (2016) identified 13 short X-ray bursts be-

wanghh@hust.edu.cn, lupin@unist.ac.kr, takata@hust.edu.cn

¹ Department of Astronomy, School of physics, Huazhong University of Science and Technology, Wuhan 430074, China

² Department of Physics, UNIST, Ulsan 44919, Korea

³ CSIRO Astronomy and Space Science, Australia Telescope National Facility, Box 76 Epping NSW 1710, Australia

⁴ Department of Astronomy, Kyoto University, Oiwakecho, Sakyo-ku, Kyoto 606-8502, Japan

⁵ Yunnan Observatories, Chinese Academy of Sciences, Kunming, 650216, China

⁶ Key laboratory for the Structure and Evolution of Celestial Objects, Chinese Academy of Sciences, Kunming, 650216, China

[†] JSPS International Research Fellow

tween 2016 July 26 and 28, with an estimate of the total energy released of $E \sim 10^{42}$ erg. The pulsar also underwent a large glitch immediately after the start of the 2016 outburst (Archibald et al. 2016). Following the X-ray outburst, monitoring of this source was carried out in radio and X-ray bands.

Following the glitch, the pulsed radio emission disappeared for about two weeks, and the reappearance of the pulse profile exhibited a multi-component structure at 2.3 GHz and a single peak at 8.4 GHz (Majid et al. 2017; Dai et al. 2018). After the glitch, the spin-down rate rapidly increased by a factor of 5–10 on 2016 September 1 (MJD ~ 57632) before recovering toward the pre-burst rate over the following three months (Dai et al. 2018; Archibald et al. 2018; Lin et al. 2018). Moreover, the radio flux increased by a factor of ten, and then started decreasing at around MJD 57632, which showed an obvious correlation with the evolution of the spin-down later after the outburst (Figure 1). During the rapid evolution of the spin-down rate, the radio pulse profile changed twice, on 2016 August 12 (MJD ~ 57612) and 29 (MJD ~ 57630). We note that the increase of the spin-down rate became faster at around August 12, and the spin-down rate began recovery to pre-glitch levels around August 29. (Archibald et al. 2017) also identified three short X-ray outbursts coincident with the suppression of the radio flux on 2016 August 30. Many of these trends are depicted in Figure 1. The Radio timing solutions shown in Figure 1 were also presented in Dai et al. (2018), formed using observations with the Parkes telescope using an observing bandwidth of 256 MHz centered at 1369 MHz.

In X-rays, Archibald et al. (2018) find the luminosity after the outburst reaches $L_X \sim 4 \times 10^{35}$ erg s $^{-1}$, which corresponds to $\sim 17\%$ of the spin-down power, suggesting the energy source of the emission is the dissipation of magnetic energy. Moreover, they also report a hardening of the spectrum and an increase in the 0.7–2.5 keV (2.5–10 keV) pulsed fraction from $\sim 38\%$ ($< 10\%$) before the outburst to $\sim 71\%$ ($\sim 56\%$). Lin et al. (2018) investigated the high-energy emission features after the X-ray outburst, and they report that the X-ray emission in 2016 August can be described by two thermal components of different spatial sizes plus a power-law component with a photon index $\Gamma \leq 1$ (see also Archibald et al. (2018)). This hard photon index above 10 keV is similar to magnetar emission (Enoto et al. 2017), rather than that of normal pulsars, for which a typical photon index ~ 1.5 is thought to originate from synchrotron radiation from secondary electron/positron pairs created by the pair-creation process. It is likely that the X-ray outburst of PSR J1119–6127 and emission after its outburst operated under a magnetar-like process. Blumer et al. (2017) report that a single power-law model with a photon index of ~ 2 is sufficient to model the X-ray spectrum taken from the *Chandra* observation at the end of 2016 October, while Lin et al. (2018) and Archibald et al. (2018) both fit the *XMM-Newton* data in 2016 December with a composite model of a single power-law plus two blackbody and one-temperature blackbody component, respectively. These multi-wavelength observations help constrain the theoretical interpretation for the mechanism of the X-ray outburst of the magnetars and high-B

TABLE 1
X-RAY OBSERVATIONS OF PSR J1119–6127

ObsID	date	instrument	Duration(ks)
<i>Swift</i>			
00034632007	2016 Aug. 09	XRT/WT	57.6
<i>XMM-Newton</i>			
0741732601	2016 Aug. 06	PN	20.1
0741732701	2016 Aug. 15	PN	27.9
0741732801	2016 Aug. 30	PN	32.5
0762032801	2016 Dec. 13	PN	47.5
<i>NuSTAR</i>			
80102048004	2016 Aug. 05	FPM A/B	127
80102048006	2016 Aug. 14	FPM A/B	170.8
80102048008	2016 Aug. 30	FPM A/B	166.5
80102048010	2016 Dec. 12	FPM A/B	183.3

pulsars.

In this paper, we revisit the emission characteristics of PSR J1119–6127 after the 2016 outburst and discuss their implications, based on multi-wavelength (radio/X-ray/GeV gamma-ray) observations. We perform spectral and timing analyses beyond those of previous studies. Specifically, we analyze phase-resolved spectra above 10 keV with *NuSTAR* data and we discuss the contribution of hard non-thermal emission to the on-pulse and off-pulse emission. We examine the relation of the radio and X-ray pulsed peaks, which were aligned with each other observations before the 2016 outburst (Parent et al. 2011; Ng et al. 2012). We also perform a spectral and timing analysis of *Fermi* Large Area Telescope (LAT)⁸ data to investigate any possible change of the GeV emission before and after the 2016 outburst.

This paper is organized as follows. In section 2, we introduce the reduction of the radio, X-ray and *Fermi* data for this study. We study the phase-resolved X-ray spectroscopy in section 3.1 and compare the phase shift between the radio and X-ray pulse peaks. We confirmed the gamma-ray pulsation after the 2016 X-ray outburst and compared the pulse shape and spectrum before and after the outburst in section 3.4. In section 4, we discuss the evolution of PSR J1119–6127 after the outburst within the framework of the twisting magnetosphere model (Beloborodov 2009).

2. DATA REDUCTION

2.1. X-ray data

For X-ray data analysis, we use archival data from the *Neil Gehrels Swift Observatory* (*Swift*), *X-ray Multi-Mirror Mission* (*XMM-Newton*) and *Nuclear Spectroscopic Telescope Array* (*NuSTAR*) taken in 2016 August and December after the outburst. Details of observations considered in this study are listed in the Table 1. For the timing analysis in the X-ray band, all events are corrected to the barycenter using the X-ray position (R.A., Decl.) = (11^h19^m14.26^s, -61°27′49.3″) and the JPL DE405 solar system ephemeris, and the local timing ephemeris was determined by maximizing the H test statistic value (De Jager & Büsching 2010).

For *Swift*, we use data in windowed timing mode with a time resolution of 1.8 ms carried out by XRT on August 9 and compare the X-ray with radio pulse profiles taken on

⁸ <https://fermi.gsfc.nasa.gov/ssc/>

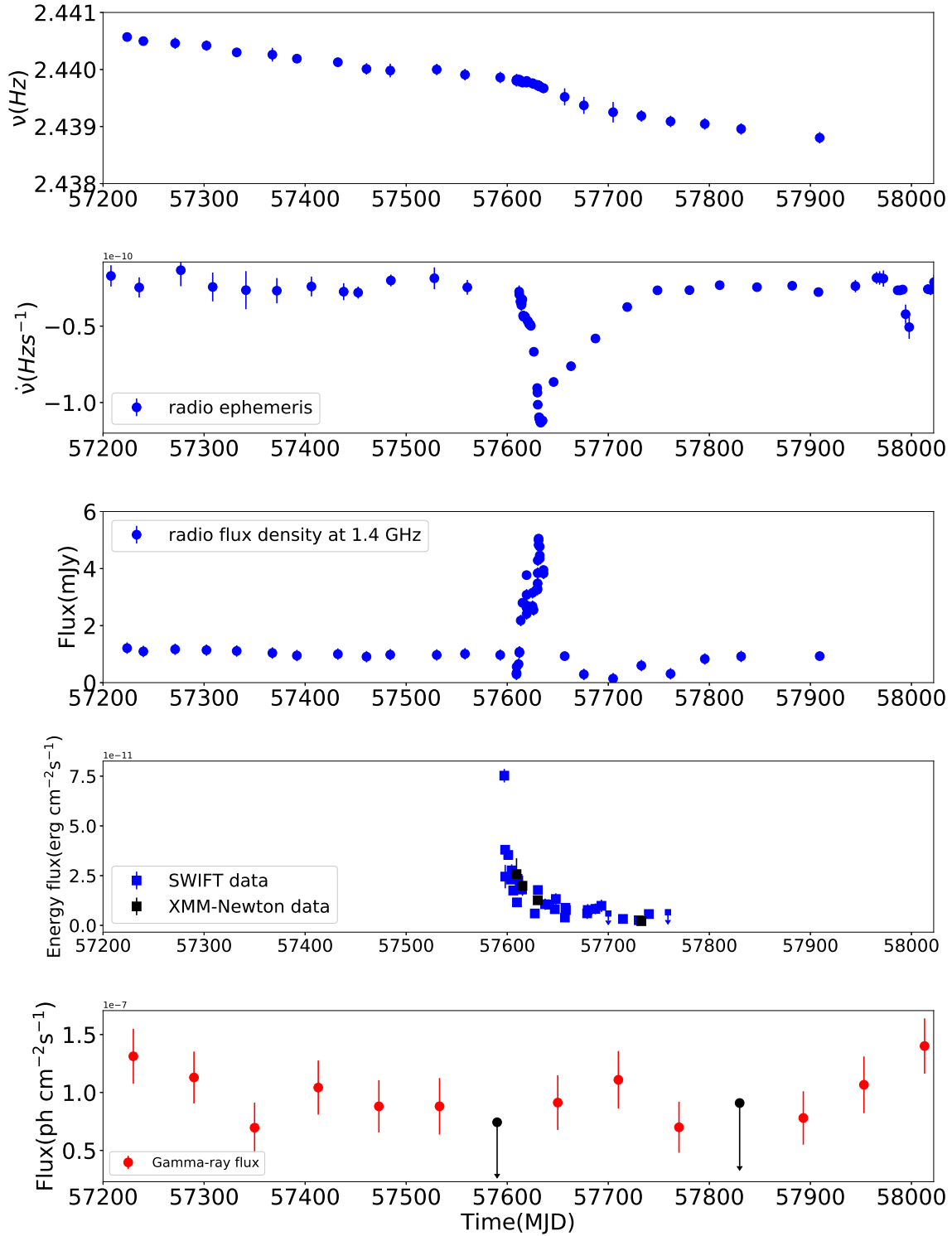


FIG. 1.— From top to bottom, the panels show evolution of the spin frequency, spin-down rate, radio flux density, X-ray flux and >0.1 GeV flux of PSR J1119–6127, respectively. In the bottom panel, each point represents the flux >0.1 GeV assessed from a 60 day accumulation of *Fermi* data, and the black arrow indicates a 3σ flux upper limit.

the same day (section 3.2). We extract the source counts from a box region of $15'' \times 35''$. Only photon energies in the range of 0.3–10 keV with grades 0–2 are included, totalling ~ 1400 source counts for further analysis.

For *XMM-Newton*, we perform the data reduction using Science Analysis Software (SAS version 16.0) and the latest calibration files. In this study, we only analyze the PN data (Large Window mode), and we process the data in the standard way using the SAS command *epproc*. We generate a Good Time Interval (GTI) file with the task *tabgtigen* and filter events with the option “RATE \leq 0.4”. We also filter out artifacts from the calibrated and concatenate the dataset with the events screening criteria “FLAG=0”. We extract source photons from a circular aperture of $20''$ centered at the nominal X-ray position (R.A., Decl.) = ($11^{\text{h}}19^{\text{m}}14.26^{\text{s}}$, $-61^{\circ}27'49.3''$), and we select the data in 0.15–12 keV energy band. We obtain ~ 26000 counts for Aug. 6 and Aug. 15, ~ 20000 counts for Aug. 30, and ~ 5890 counts for Dec. 13, respectively, from the source region.

For *NuSTAR* data analysis, we use the script *nuproducts* provided by HEASoft, which runs automatically in sequence all the tasks for the standard data reduction, and we use the data taken with the Focal Plane Modules A and B (FPM A/B). We generate source and background extraction region files using DS9 by choosing a circular region of $\sim 50''$ radius centered on the source and the background region close to the source, respectively. All required event files and spectral files in this study are obtained with the task *nuproducts* and we obtained ~ 20500 counts for Aug. 6, ~ 16000 for Aug. 15, ~ 10500 counts for Aug. 30, and ~ 2400 counts for Dec. 13.

To perform the phase-resolved spectroscopy, we define an on-pulse and off-pulse phase for each *XMM-Newton* and *NuSTAR* observation, as shown in Figure 2. For the *XMM-Newton* data, we extract the events of on/off pulse phase using the phase information obtained from the *efold* command.

For the *NuSTAR* data, we create Good Time Interval (GTI) files for on-pulse and off-pulse phases that are identical with the phase-interval for *XMM-Newton*, and apply the GTI files to *nuproduct* task with the “usrgti-file” parameter. We group the channels so as to achieve a signal-to-noise ratio $S/N = 3$ in each energy bin for *XMM-Newton* PN data and at least 30 counts per bin for *NuSTAR* FPM A/B data. We carry out the spectral analysis with the XSPEC version 12.9.1.

2.2. Fermi data

We use *Fermi* Large Area Telescope (LAT)(Atwood et al. 2009) Pass 8 (P8R2)(Atwood et al. 2013) data with the source centered at RA= $11^{\text{h}}19^{\text{m}}14^{\text{s}}.3$, Decl.= $-61^{\circ}27'49''.5$ (J2000), the radio coordinates of the pulsar (Safi-Harb & Kumar 2008), with an uncertainty of $0''.3$. We selected “Source” class events (evclass= 128) and collected photons from the front and back sections of the tracker (i.e., evttype = 3). The data quality is further constrained by restriction to instrument good time intervals (i.e., DATA_QUAL > 0), and we also remove events with zenith angles larger than 90° to reduce gamma-ray contamination from the earth’s limb.

In our spectral analysis, we construct a background emission model, including the Galactic diffuse emission (gll_iem_v06) and the isotropic diffuse emission

(iso_P8R2_SOURCE_V6_v06) circulated by the *Fermi* Science Support Center, and all 3FGL catalog sources (Acero et al. 2015) within 10° of the center of the region of interest. The phase-averaged spectrum was obtained using the *Fermi* Science Tool “gtlike” to perform a binned likelihood analysis of data in the energy range 0.1–300 GeV and within a 20° radius region of interest (ROI) centered on the pulsar position.

In order to investigate the change of the spectra, we generate the phase-averaged spectra for three epochs determined by the spin-down behavior and GeV flux evolution: pre-outburst epoch (MJD 57023 to MJD 57570), outburst/relaxation epoch (MJD 57570 to MJD 57815) and post-relaxation epoch (MJD 57815 to MJD 58482).

For the timing analysis, we consider photons within a 2-degree aperture, which contains most of the significant source photons. We use photon weighting to increase the sensitivity of pulsation statistics (Kerr 2011). Using the results of the likelihood analysis, we used the *gtdiffresp* and *gtsrcprob* tools to assign a probability to each photon that it originated from the pulsar. Assigning phases to photons is accomplished with the *Fermi* plugin for TEMPO2. We obtain 39,045 counts in 0.1–300 GeV between MJD 57870–58380, while the total weighted photon count is only 1131.2, indicating the aperture is dominated by background. All the photon arrival times were corrected to the barycentric dynamical time (TDB) with the JPL DE405 solar system ephemeris with the task *gtbary*. The high-order polynomial terms of the timing ephemerides mentioned in section 3.4 are used to describe the complicated timing noise.

3. RESULTS

3.1. Phase-resolved spectroscopy of the X-ray data

Figures 2 and 3 show the folded light curves for *XMM-Newton* and *NuSTAR* observations, respectively, produced as described in §2.1. In each panel, we indicate the definition of the on-pulse and off-pulse phases for phase-resolved spectroscopy.

Figures 4 and 5 show the observed spectra for on-pulse and off-pulse phases, respectively. **Due to the similar observational time covered by the *XMM-Newton* and *NuSTAR* data, we therefore perform a joint spectral fit of the data obtained from the two instruments. We introduced a constant in the fit to account for the cross-calibration mismatch and modeled photoelectric absorption in the ISM using Wisconsin cross-sections (Morrison&McCammon 1983). We fixed the constant factor of *XMM-Newton* at unity, and obtained ~ 1.11 for *NuSTAR* FPM A/B through the fitting. We use two blackbody emission components plus a power-law with a photon index (Γ) and the linked absorption of $N_H = 1.45^{+0.1}_{-0.1} \times 10^{22} \text{ cm}^{-2}$ to fit all the spectra simultaneously.** Table 2 summarizes the best-fit parameters for on-pulse and off-pulse spectra, respectively. The temperatures and radii of the 2BB components are consistent with the previous study (Lin et al. 2018), which fit the phase-resolved spectra of the *XMM-Newton* data with the 2BB model. As Table 2 shows, we find that the power-law component is required for both on- and off-pulse intervals for August data, although the 2BB model

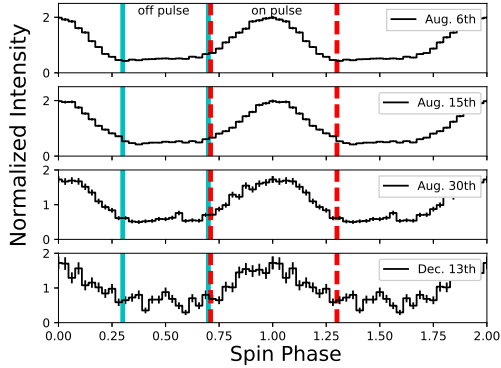


FIG. 2.— X-ray folded light curves in the 0.5–10.0 keV energy band from *XMM-Newton* on 2016 August 6, 15, 30 and December 13 from upper to bottom. The vertical green solid-lines and red dashed-lines define the off-pulse phase and on-pulse phase, respectively.

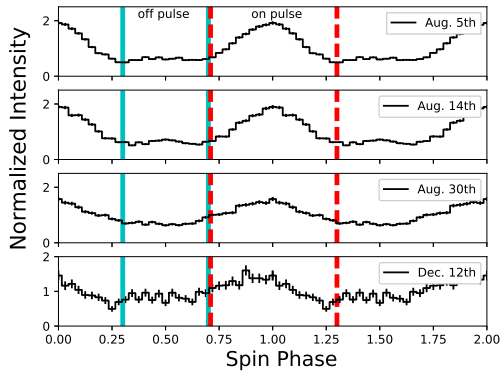


FIG. 3.— X-ray folded light curves in the 3.0–78.0 keV energy band from *NuSTAR* on 2016 August 5, 14, 30 and December 12 from upper to bottom. The vertical green solid-lines and red dashed-lines define the off-pulse phase and on-pulse phase, respectively.

sufficiently describes the spectrum of the on-pulse phase on August 15. This is likely because the blackbody emission is ~ 2 orders of magnitude brighter than the power-law component, and the contribution of the power-law component is not significant on August 15. In December, the 2BB model can provide an acceptable fit to both the on- and off-pulse spectra, and the negative power-law component is poorly constrained and therefore unreliable. Following the evolution of the observed flux in Table 2, the flux level of the power-law component decreased below the detector sensitivity by 2016 December.

The pulse profiles in the 3–78 keV band (Figure 3) are dominated by the thermal components, but they may not represent the pulsation above 10 keV, where the power-law component dominates. In fact, no significant pulsed signal was detected above 10 keV in August data (Lin et al. 2018).

3.2. Comparison between radio and X-ray pulse positions

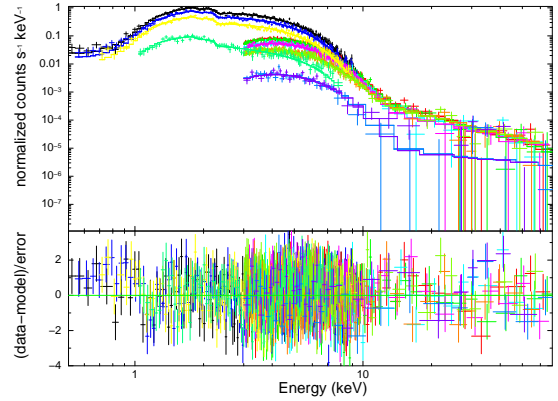


FIG. 4.— The joint spectral fits to the on-pulse spectra. In the plots, the spectra extending between 0.5–12 keV and > 3 keV represent the results for the *XMM-Newton* PN and *NuSTAR* FPM A/B data, respectively. For each instrument, the spectra from top to bottom correspond to the data from 2016 August 6 and December 12/13, respectively.

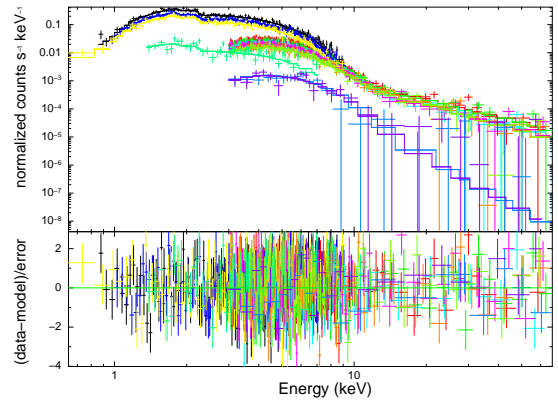


FIG. 5.— The joint fit to off-pulse spectrum. The colors are as for Figure 4.

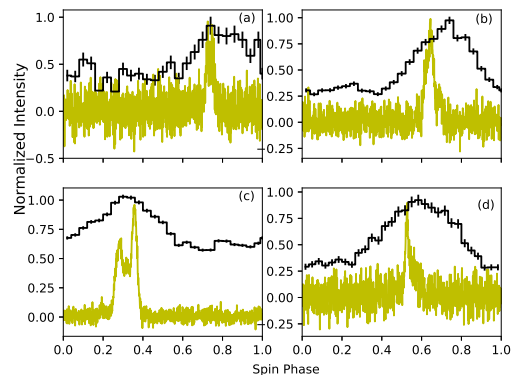


FIG. 6.— Radio (yellow lines) and X-ray (black histograms) pulse profiles of PSR J1119–6127 on 2016 (a) August 6, (b) August 15, (c) August 30 and (d) December 10 for radio and December 12/13 for X-ray. The X-ray folded light curves are obtained from *Swift* (a), *NuSTAR* (b) and *XMM-Newton* (c and d) observations. We define the phase zero (t_0) at the epoch of the radio observation (second column in Table 3).

TABLE 2
BEST-FIT SPECTRAL PARAMETERS OBTAINED FROM THE FIT TO THE
PHASE-RESOLVED SPECTRA OF THE ON-PULSE PHASE AND OFF-PULSE
PHASES.

	Aug. 5/6	Aug. 14/15	Aug. 30	Dec. 12/13
	On-pulse			
N_H^a (cm^{-2})	$1.45^{+0.1}_{-0.1} \times 10^{22}$			
kT1 (KeV)	$0.31^{+0.03}_{-0.02}$	$0.35^{+0.03}_{-0.02}$	$0.35^{+0.04}_{-0.03}$	$0.33^{+0.02}_{-0.03}$
R1 (km)	$5.76^{+1.4}_{-1.47}$	$4.28^{+1.6}_{-0.86}$	$3.7^{+0.93}_{-1.05}$	$2.28^{+0.42}_{-0.33}$
F_{BB1}^b	$0.45^{+0.6}_{-0.28}$	$0.39^{+0.4}_{-0.28}$	$0.27^{+0.37}_{-0.12}$	$0.088^{+0.08}_{-0.05}$
kT2 (KeV)	$1.0^{+0.01}_{-0.01}$	$1.02^{+0.01}_{-0.01}$	$1.02^{+0.02}_{-0.02}$	$1.08^{+0.02}_{-0.02}$
R2 (km)	$1.23^{+0.01}_{-0.01}$	$0.98^{+0.03}_{-0.03}$	$0.7^{+0.07}_{-0.07}$	$0.24^{+0.02}_{-0.02}$
F_{BB2}^b	$2.1^{+0.35}_{-0.09}$	$1.58^{+0.16}_{-0.13}$	$0.98^{+0.07}_{-0.19}$	$0.12^{+0.05}_{-0.03}$
Γ^c	$0.84^{+0.2}_{-0.39}$	$0.06^{+0.2}_{-0.2}$	$0.48^{+0.2}_{-0.2}$	$-1.01^{+0.9}_{-0.95}$
F_{po}^b	$0.027^{+0.022}_{-0.012}$	$0.006^{+0.006}_{-0.003}$	$0.014^{+0.01}_{-0.006}$	$1.15E-4^{+5E-6}_{-7E-6}$
	Off-pulse			
kT1 (KeV)	$0.35^{+0.06}_{-0.04}$	$0.32^{+0.05}_{-0.04}$	$0.32^{+0.06}_{-0.04}$	$0.37^{+0.001}_{-0.001}$
R1 (km)	$2.86^{+1.5}_{-0.7}$	$3.07^{+1.8}_{-1.1}$	$2.65^{+1.7}_{-1.1}$	$0.77^{+0.77}_{-0.8}$
F_{BB1}^b	$0.18^{+0.7}_{-0.15}$	$0.13^{+0.5}_{-0.1}$	$0.11^{+0.58}_{-0.08}$	$0.016^{+0.2}_{-0.016}$
kT2 (KeV)	$1.05^{+0.02}_{-0.02}$	$1.06^{+0.02}_{-0.02}$	$1.03^{+0.03}_{-0.03}$	$1.2^{+0.1}_{-0.1}$
R2 (km)	$0.65^{+0.2}_{-0.3}$	$0.55^{+0.33}_{-0.22}$	$0.48^{+0.18}_{-0.2}$	$0.11^{+0.02}_{-0.02}$
F_{BB2}^b	$0.78^{+0.12}_{-0.18}$	$0.59^{+0.1}_{-0.09}$	$0.44^{+0.1}_{-0.1}$	$0.04^{+0.04}_{-0.02}$
Γ^c	$0.51^{+0.3}_{-0.2}$	$0.53^{+0.43}_{-0.37}$	$0.89^{+0.42}_{-0.37}$	$3.11^{+0.92}_{-1.992}$
F_{po}^b	$0.03^{+0.011}_{-0.008}$	$0.02^{+0.006}_{-0.018}$	$0.03^{+0.015}_{-0.015}$	$0.042^{+0.03}_{-0.0001}$
χ^2_ν /D.O.F.	1.15/2478			

^a The absorption column density.

^b The unabsorbed flux is measured in 0.5-10.0 keV and recorded in units of 10^{-11} erg cm^{-2} s $^{-1}$.

^c Photon index of the power-law model.

TABLE 3
EPHEMERIS OF RADIO AND X-RAY

	radio/ t_0 (MJD)	X-ray (MJD)	Instrument	f_0 (Hz)	f_1 (Hz \cdot s $^{-1}$)
Aug. 9	57609.19	57609.16-57609.83	<i>Swift</i>	2.439814	–
Aug. 15	57615.07	57614.50-57615.50	<i>NuSTAR</i>	2.4397973	–
Aug. 30	57630.17	57630.12-57630.52	<i>XMM</i>	2.4397218	–
Dec. 10-13	57732.72	57735.38-57735.94	<i>XMM</i>	2.43918	-2.507E-11

Prior to the 2016 outburst, the X-ray pulse peak was aligned with the radio pulse peak (Ng et al. 2012). In this study, therefore, we compare radio pulse profiles reported in Dai et al. (2018) with X-ray pulse profiles taken in 2016 August and December. Here we used radio observations with the Parkes telescope taken on August 9, 15, 30 and December 10, all of which have an observing bandwidth of 256 MHz centred at 1369 MHz. Details of the observations and data reduction can be found in Dai et al. (2018). Owing to a rapid change in the spin-down rate, it is not practical to create a single global ephemeris spanning from August to December. Instead, we use a local timing solution determined from each X-ray observation according to the maximum H-test value yielded in a periodicity search. In our analysis, the radio observations are each spanned by a single X-ray observation at the August 6, 15, and 30 epochs, so that the spin frequency f_0 obtained from the X-ray observation can be used to fold the corresponding radio data. However, in December, the radio and X-ray observations are separated by about two days, necessitating the application of

a f_1 component in the timing solution used to fold the radio data. Table 3 summarizes the local ephemerides used in this study, where we define the epoch/phase zero (t_0) near the epoch of the radio observation (second column in Table 3).

To compare with the radio and X-ray peak positions in 2016 December, we generate a reference f_0 and f_1 from the information of the local spin frequency determined by the radio observations in 2016 December and 2017 January, assuming that the spin-down rate in 2016 December is stable as reported by Dai et al. (2018). To correctly align the radio data, for each radio observation we created an artificial pulse time-of-arrival (TOA) corresponding to the reference epoch in Table 3, and we likewise used a model of the radio pulse profile (template) to measure the radio TOA at the observatory. By measuring the offset between these TOAs with TEMPO2 (Hobbs, Edwards & Manchester 2006), we obtained the correct value by which to rotate the radio profile. In this way, all effects of dispersion and light travel time between the barycenter and the Parkes telescope are ac-

counted for. On the other hand, the barycentered X-ray timestamps are simply folded by the ephemerides in Table 3 such that the epoch represents pulse phase 0.

Figure 6 compares the pulse profiles of the X-ray and radio emission. We find there is no significant evolution in X-ray and radio peak phasing following the X-ray outburst. Moreover, the X-ray light curve consists of one single and broad peak with which the radio peak is roughly aligned, similar to the pre-outburst configuration (Ng et al. 2012). Even so, the observed X-ray flux remained an order of magnitude higher than that preceding the outburst (Figure 11).

3.3. Fermi-LAT long term light curve and spectra

The first panel of Figure 7 shows the light curve (>0.1 GeV) between MJD 57023 and 58482 obtained with the standard binned maximum likelihood analysis. We divide the entire time range into 60 day time bins, and we measure an average photon flux of $\sim 9.5 \times 10^{-8}$ cts $\text{cm}^{-2} \text{s}^{-1}$. The time-averaged photon fluxes for three epochs are $F = (1.0 \pm 0.5) \times 10^{-7}$ cts $\text{cm}^{-2} \text{s}^{-1}$ for the pre-outburst epoch, $F = (0.7 \pm 0.2) \times 10^{-7}$ cts $\text{cm}^{-2} \text{s}^{-1}$ for outburst/relaxation epoch, and $F = (1.0 \pm 0.6) \times 10^{-7}$ cts $\text{cm}^{-2} \text{s}^{-1}$ for the post-relaxation epoch.

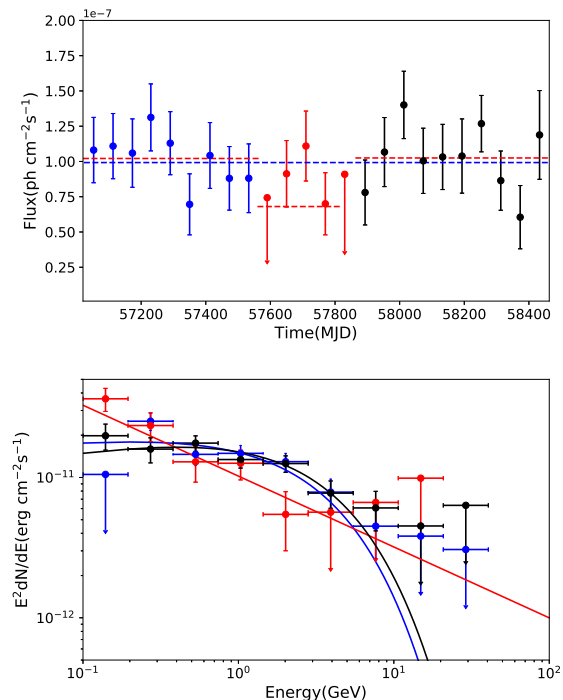


FIG. 7.— Evolution of the > 0.1 GeV flux of PSR J1119-6127 (upper panel). The light curve is generated with $\Gamma_2=1$, the blue dashed line shows the time-averaged flux and the red horizontal lines indicate the averaged fluxes for three epochs. Phase-averaged spectra for three epochs (lower panel). Blue: pre-outburst (MJD 57023 to MJD 57570). Red: relaxation (MJD 57570 to MJD 57815). Black: post-relaxation (MJD 57815 to MJD 58482).

The lower panel shows the corresponding gamma-ray spectra for the three epochs (Figure 7), **which are mod-**

eled by a power-law with an exponential cut-off:

$$dN/dE = N_0(E/E_0)^{-\Gamma_1} \exp[-(E/E_C)^{\Gamma_2}], \quad (1)$$

where dN/dE is the differential photon rate per unit energy, time, and area, N_0 is a normalization constant, E_0 is the energy scale factor, Γ_1 is the spectral power-law index, E_C is the cutoff energy, and Γ_2 is the exponential index. We obtain the best fitting parameters $(E_C, \Gamma_1, \Gamma_2) \sim (2.6 \pm 0.4 \text{ GeV}, 1.9 \pm 0.07, 0.83 \pm 0.02)$ for the pre-outburst epoch, $(2.2 \pm 0.3 \text{ GeV}, 2.5 \pm 0.12, 0.005 \pm 0.001)$ for the outburst/relaxation epoch and $(2.6 \pm 0.25 \text{ GeV}, 1.92 \pm 0.09, 0.8 \pm 0.02)$ for the post-relaxation state (see Table 4). We confirm in Figure 7 that the phase-averaged spectrum in the post-relaxation epoch is consistent with that of pre-outburst epoch. For the outburst/relaxation state, a very small exponential index ($\Gamma_2 \sim 0.005$) indicates that a power law function is enough to describe the observed spectra. We also fit the spectra with a pure exponential cut-off function ($\Gamma_2 = 1$) and obtained the fitting parameters of $(E_C, \Gamma_1) = (3.1 \pm 0.45 \text{ GeV}, 1.82 \pm 0.06)$ for the pre-outburst epoch, $(2.3 \pm 0.23 \text{ GeV}, 2.16 \pm 0.21)$ for the outburst/relaxation epoch and $(3.1 \pm 0.35 \text{ GeV}, 1.85 \pm 0.09)$ for the post-relaxation epoch, respectively. These spectral analyses show the GeV emission during the outburst/relaxation state is significantly softer than “steady spectra” obtained in pre-outburst and post relaxation states.

3.4. Gamma-ray pulsation

Due to the complicated spin-down rate recovery and flux variability described in §2.2, we are unable to either construct a coherent pulsar timing solution with which to fold gamma-ray data or to recover the gamma-ray pulsations in a “blind search” over parameters. Instead, we restrict our pulsation search and characterization to the “post-relaxation” period following MJD 57815. Using Parkes observations and the resulting pulse times-of-arrival (TOAs), we are able to adequately model the pulsar spin evolution with the ephemeris tabulated in the right column of Table 5, whose parameters were optimized using TEMPO2. Additionally, we used pre-outburst radio observations to build a long-term ephemeris (left column).

Using these ephemerides, we folded the gamma-ray data using photon weights (Kerr 2011) to enhance the pulsed signal. Fig. 8 presents the resulting 0.1–300 GeV pulse profiles of PSR J1119–6127 and compares the pulse profile in pre-outburst and post-relaxation stages. No significant change of the pulse profile was found. Fig. 9 compares the pulse profiles between gamma-ray and radio emission after the X-ray outburst, MJD 57872–58378. We find that the radio peak precedes the main gamma-ray peak by ~ 0.4 cycle. In the previous studies before the X-ray outburst (Parent et al. 2011), it is found that the measurement of phase shifts between the gamma-ray peak and radio peak is similar to our detection. Since the spin-down rate and gamma-ray emission properties measured after MJD 57800 have

TABLE 4
PARAMETERS OF SPECTRAL FITTING OF THREE EPOCHS

Epochs	Pre-outburst	Outburst/Relaxation	Post-relaxation
MJD	57023-57570	57570-57815	57815-58482
Flux(10^{-7} cts cm^{-2} s^{-1})	1.02 ± 0.49	0.8 ± 0.25	1.02 ± 0.50
Cutoff Energy (GeV)	2.6 ± 0.4	2.2 ± 0.3	2.6 ± 0.25
Photon index (Γ_1)	1.9 ± 0.07	2.5 ± 0.12	1.92 ± 0.09
Exponential index (Γ_2)	0.83 ± 0.02	0.005 ± 0.001	0.8 ± 0.02

recovered to those before the X-ray outburst, the re-configuration of the magnetosphere after X-ray outburst was complete before MJD 57800. The same phase shift measured between the radio peak and gamma-ray peak suggests that a steady magnetospheric structure established after the 2016 X-ray outburst is similar to that before the outburst event. We also checked the *NICER* data taken during the valid MJD range of the ephemeris; however, we could not obtain a significant pulsation. This is probably owing to the high flux level of the background emission.

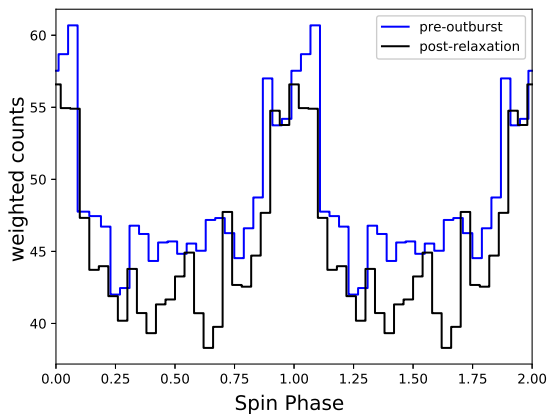


FIG. 8.— Gamma-ray pulse profile of PSR J1119–6127 obtained in pre-outburst (MJD 56980-57480) and in post-relaxation (MJD 57872-58379). We obtained the light curve from the weighted photons folded with the ephemerides listed in Table 5. The peak positions are shifted to phase zero to compare the pulse structures in two stages, and two cycles of the profile are shown for clarity.

4. DISCUSSION

The magnetar XTE J1810–197, with a surface magnetic field of $B_s \sim 3 \times 10^{14}$ G (Ibrahim et al. 2004; Weng et al. 2015), underwent an X-ray outburst in 2003 and emitted pulsed radio emission following the outburst. The evolution of the timing solution, radio emission and X-ray emission properties of PSR J1119–6127 after its 2016 outburst are very similar to those of XTE J1810–197, although the recovery time scale (τ_r) and released total energy (E_{tot}) are one or two orders of magnitude smaller: $\tau_r \sim 0.5$ yr and $E_{tot} \sim 10^{42}$ erg for PSR J1119–6127, and $\tau_r \sim 3$ yr and $E_{tot} \sim 10^{43-44}$ erg for XTE J1810–197 (Camilo et al. 2006). After the outburst, the spin-down rate increased with a time scale of ~ 30 d for PSR J1119–6127 and of ~ 2 yr for XTE J1810–197, and then recovered toward the steady state values over a time scale ~ 100 d for PSR J1119–6127 and with ~ 3 yr for XTE J1810–197.

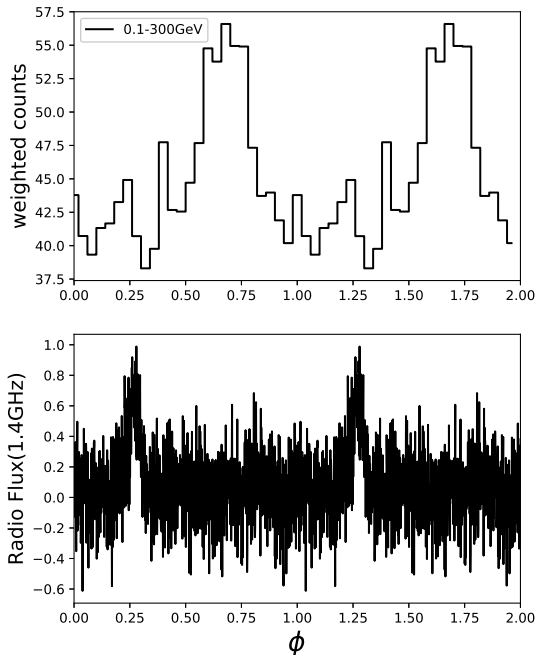


FIG. 9.— The pulse profiles in >0.1 GeV gamma-ray (top panel) and radio (1.4GHz) bands after MJD 57872 (2017 April), which is ~ 9 months after the X-ray outburst/glitch. The phase zero in each panel refers to MJD 57935.25.

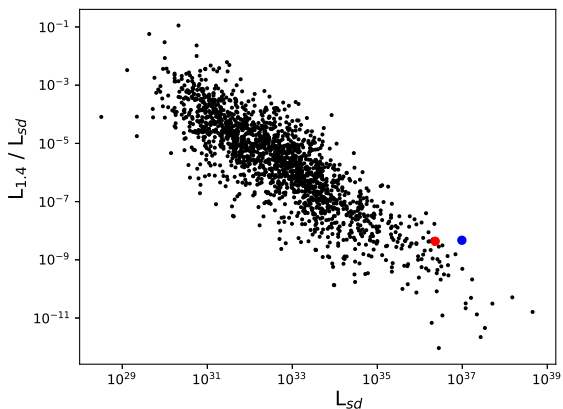


FIG. 10.— Relation between spin-down power and radio luminosity at 1.4 GHz of the known pulsars. The data come from the <https://www.atnf.csiro.au/research/pulsar/psrcat/>. The red and blue dots are used to denote PSR J1119–6127 in the normal stage and soon after its 2016 outburst.

TABLE 5
LOCAL EPHEMERIS OF PSR J1119–6127 DERIVED THROUGH TOA ANALYSIS THROUGH *Fermi* ARCHIVE.

Parameter	PSR J1119–6127	
Pulsar name	PSR J1119–6127	
Valid MJD range	56254.719–57495.308	57872–58378
Right ascension, α	11:19:14.3	
Declination, δ	-61:27:49.5	
Pulse frequency, ν (s^{-1})	2.444203(5)	2.438745779(1)
First derivative of pulse frequency, $\dot{\nu}$ (s^{-2})	$-1.81(7) \times 10^{-11}$	$-2.46635(3) \times 10^{-11}$
Second derivative of pulse frequency, $\ddot{\nu}$ (s^{-3})	$-3.7(6) \times 10^{-19}$	$-1.83(2) \times 10^{-20}$
Third derivative of pulse frequency, $\nu^{(3)}$ (s^{-4})	$1.9(4) \times 10^{-26}$	$1.604(4) \times 10^{-26}$
Fourth derivative of pulse frequency, $\nu^{(4)}$ (s^{-5})	$-8(2) \times 10^{-34}$	$-6.11(2) \times 10^{-33}$
Fifth derivative of pulse frequency, $\nu^{(5)}$ (s^{-6})	$2.8(9) \times 10^{-41}$	$1.639(4) \times 10^{-39}$
Sixth derivative of pulse frequency, $\nu^{(6)}$ (s^{-7})	$-7(2) \times 10^{-49}$	$-3.13(2) \times 10^{-46}$
Seventh derivative of pulse frequency, $\nu^{(7)}$ (s^{-8})	$1.1(6) \times 10^{-56}$	$3.89(8) \times 10^{-53}$
Eighth derivative of pulse frequency, $\nu^{(8)}$ (s^{-9})	$-9(4) \times 10^{-65}$	$-2.36(9) \times 10^{-60}$
Epoch of frequency determination (MJD)	55440	57935.25
Time system	TDB	
RMS timing residual (μs)	1204.41	28861.388
Number of time of arrivals	42	39

Note: the numbers in parentheses denote errors in the last digit

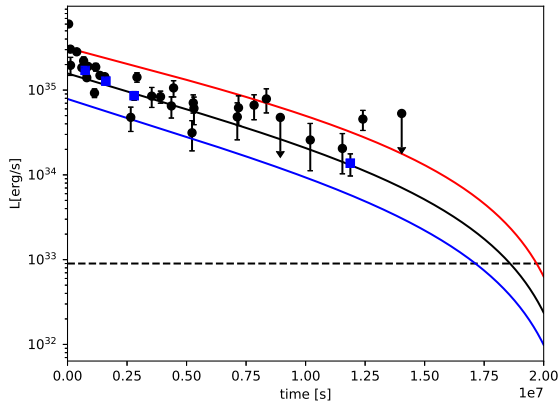


FIG. 11.— Evolution of the X-ray luminosity after 2016 outburst, **The inferred luminosity** by *Swift* (black point) and *XMM-Newton* (blue square) is calculated by assuming the solid angle of 4π . The solid lines show the model curve predicted by the twisting magnetosphere (Beloborodov 2009), assuming $\mu = 5 \times 10^{31} \text{ G} \cdot \text{cm}^3$, the initial twist angle of $\phi_0 = 0.25$ and the initial polar angle of the j-bundle of $u_0 = 0.4$. In addition, the electric potential drop is assumed to be $V_e(u) = V'(u_0 - u) + V_0$ with $V' = 2.5 \times 10^9 \text{ V}$ and $V_0 = 10^{10} \text{ V}$ for red line, $V_0 = 5 \times 10^9 \text{ V}$ for black line and $V_0 = 2.5 \times 10^9 \text{ V}$ for blue line. **The horizontal dash line shows the persistent emission luminosity** $L_X \sim 9 \times 10^{32} \text{ erg s}^{-1}$

XTE J1810–197 was known to have radio pulsations (Camilo et al. 2006). The radio emission from the magnetar disappeared in 2008 and reappeared in late 2018 along with an X-ray enhancement (Dai et al. 2019; Gotthelf et al. 2019). This 2018 XTE J1810–197 outburst shows similarities to the 2003 outburst in terms of X-ray flux, spectrum, and pulse properties. Likewise, the spectra can be fit by two blackbodies plus an additional power-law component to account for emission above 10 keV. Moreover, Gotthelf et al. (2019) find that the pulse peak of the X-rays lags the radio pulse by ~ 0.13 cycles, which is almost exactly as the behavior of the 2003 outburst. Both XTE J1810–197 and PSR J1119–6127 showed a continuous decrease of the X-ray emission after

the outburst. The similarities between these two pulsars support the identification of the 2016 X-ray outburst of PSR J1119–6127 as magnetar-like activity.

One interesting observational property after the X-ray outburst is the evolution of the radio emission and spin-down rate (Figure 1); (i) the flux evolution of the radio emission is correlated with the spin-down rate evolution and (ii) an additional component of the radio emission appeared in 2016 August/September (Majid et al. 2017; Dai et al. 2018). An additional component was also observed after previous glitches (Weltevrede et al. 2011a; Antonopoulou et al. 2015). Figure 10 plots the efficiency of the 1.4 GHz radiation ($\eta = L/L_{sd}$) and the spin-down power for the rotation powered pulsars, for which the data are taken from the ATNF pulsar catalog (Manchester et al. 2005) and the radio luminosity is calculated from $L_{1.4} = S_{1400} d^2$ with d being the distance to the source; the red and blue dots represent PSR J1119–6127 ($d = 8.4 \text{ kpc}$) in its baseline stage and at the end of 2016 August, respectively.

The evolution of the radio emission and spin-down rate after the X-ray outburst might be a result of the reconfiguration of the global magnetosphere (current structure and/or dipole moment strength) caused by, for example, crustal motion driven by the internal magnetic stress (Beloborodov 2009; Huang et al. 2016). The appearance of new radio components after the X-ray outburst may be a result of the change of the structure of the open magnetic field region. For example, the radio intensity increased by about a factor of 5 in 2016 August after X-ray outburst. **We suppose this extra component exists** but does not point toward the observer in the normal state. In such a case, the radio efficiency of this pulsar would be much higher than other pulsars having similar spin-down power unless the distance is less than $d = 8.4 \text{ kpc}$, since the apparent efficiency in the normal state is already higher than typical values, as Figure 10 shows. It is also possible that the extra radio component appearing after the X-ray outburst originates from a new emission region created after the outburst, and plasma flow on the new open field lines would produce the extra

radio emission after X-ray outburst. The evolution of the spin-down rate and the radio/GeV emission relationship suggest that the re-configuration of the global magnetosphere at most continued for six months after the X-ray outburst and the structure returned to the pre-outburst state by about 2016 December.

Figure 11 shows the evolution of the X-ray luminosity (by assuming $d = 8.4\text{kpc}$) after the X-ray outburst. The X-ray luminosity gradually decreased after the outburst, and the source was undetected by *Swift* observations in 2017. In the twisted magnetosphere model (Beloborodov 2009), for example, the timescale of the evolution of the magnetosphere (t_t) is related to the evolution of the current j -bundle, and it is estimated as

$$t_t = \frac{\phi_0 u \mu}{c R_{NS} V_e} = 0.33\text{yr} \\ \times \left(\frac{\phi_0}{0.25} \right) \left(\frac{u}{0.4} \right) \left(\frac{\mu}{5 \cdot 10^{31} \text{G cm}^3} \right) \left(\frac{V_e}{5 \cdot 10^9 \text{V}} \right)^{-1} \quad (2)$$

where $\phi_0 \sim B_t/B$ is the twist angle with B_t being the toroidal field, $u = \sin^2 \theta$ with θ is the polar angle of the current j -bundle, $R_{NS} = 10^6\text{cm}$ is the neutron star radius and μ is the magnetic dipole moment. In addition, V_e is the voltage to maintain the twist current, which is expressed by $I_e \sim \mu c \phi_0 u^2 / 2R_{NS}^2$. The induced electric potential may be on the order of $10^9\text{V} - 10^{10}\text{V}$, which can produce GeV electrons that resonantly scatter X-ray to GeV gamma rays that are eventually converted into electron/positron pairs (Beloborodov 2009). The radiation luminosity, which is $L_t \sim I_e V_e$, is estimated to be

$$L_t \sim 2.5 \times 10^{35} \text{erg/s} \\ \times \left(\frac{\phi_0}{0.25} \right) \left(\frac{u}{0.4} \right)^2 \left(\frac{\mu}{5 \cdot 10^{31} \text{G cm}^3} \right) \left(\frac{V_e}{5 \cdot 10^9 \text{V}} \right). \quad (3)$$

Luminosity is roughly proportional to $(t - t_t)^2$ (Beloborodov 2009). The solid lines in Figure 11 show examples of the evolution of the X-ray luminosity with particular parameters (e.g., twist angle and potential drop), for which we apply Eq. (37) in Beloborodov (2009) to calculate the temporal evolution of the j -bundle. This model suggests that the X-ray emission powered by the untwisting magnetosphere dominates the persistent emission, $L_X \sim 9 \times 10^{32} \text{erg s}^{-1}$ (horizontal dashed line in Figure 11), until $\sim 0.6\text{yr}$ after the outburst.

Although the X-ray spectrum requires two blackbody components, the pulse profile shows a single broad peak after the X-ray outburst, indicating that the emission regions of the two components should be close to each other. In fact, some young pulsars and millisecond pulsars also show two-blackbody emission from the heated polar cap, in the form of core (high-temperature and smaller emission region) and rim (low-temperature and wider emission region) components, respectively (Takata et al. 2012). While the incoming particles heat a part of the stellar surface upon impact, they also emit high-energy photons toward the stellar surface. Since the local magnetic field line has a curvature, the radiation heats a surface area wider than that heated by the bombardment of the incoming particles. We therefore speculate that two-black body emission of PSR J1119–6127

might also be due to the photon-pair shower, namely, impact of incoming particles (umbra) and illumination by incoming radiation (penumbra).

As presented in sections 3.3 and 3.4, the GeV emission in the relaxation state is probably suppressed due to strong X-ray emission that increases the optical depth of the photon-photon pair-creation process and/or due to a reconfiguration of the magnetosphere. The GeV emission properties (pulse shape, spectrum and phase lag from the radio peak) taken after 2016 December, on the other hand, are consistent with those before the X-ray outburst. These results indicate that the 2016 X-ray outburst and subsequent reconfiguration of the magnetosphere did not permanently change the structure of the GeV emission region. The phase-averaged spectra in the pre-outburst and post-relaxation states can be fitted by the power-law with sub-exponential cut-off ($\Gamma_2 \sim 0.8$) model. This sub-exponential cut-off behavior is a common property for most gamma-ray pulsars (Fermi-LAT pulsar catalogue; (Abdo et al. 2013)), and it probably suggests the emission origin from the outer magnetosphere (e.g., Aliu et al. 2008; Takata et al. 2016). GeV emission from the polar cap accelerator/cascade regions is highly suppressed by the magnetic pair-creation process for the canonical pulsars, and the spectrum of such emission is expected to follow a super-exponential cutoff ($\Gamma_2 > 1$) in the 0.1-1GeV band. The observed phase lag of ~ 0.4 between the radio and gamma-ray pulse peaks of PSR J1119–6127 also suggests the GeV emission originated from the outer magnetosphere. The phase lag between the radio and gamma-ray peaks is also a common feature of the radio-loud gamma-ray pulsars, and the magnitudes distribute between 0-0.5 phase lag with most cases of only around 0.1-0.2 phase lag. The observed phase lag is anti-correlated to the gamma-ray peak separation; smaller phase lag tends to have larger gamma-ray peak separation, and gamma-ray pulsars with a larger phase lag, say 0.3-0.4, tend to have a single gamma-ray peak (Abdo et al. 2013).

A phase lag can be expected if the GeV emission is from the outer magnetosphere and the radio emission is from a region above the polar cap (Romani 1996). Pierbattista et al. (2016) studied the relationship of phase lag between the gamma-ray and radio peaks and the locations of the GeV and radio emission regions. Their results show that such a large phase lag for PSR J1119–6127 is difficult to reproduce if the gamma-ray emission comes from the polar cap region. They also demonstrate that the GeV emission from the outer magnetosphere is consistent with the observed relation between the phase lag and gamma-ray peak separation.

A large lag with a single gamma-ray peak of PSR J1119–6127 will be consistent with the GeV emission originated from the outer magnetosphere. For the emission from outer magnetosphere, the line of sight close to the spin equa-

tor predicts the double peak GeV light curve, while, with a smaller or larger viewing angle from the spin axes, say $\sim 45^\circ$ or 135° , it expects a single broad pulse of PSR J1119–6127 (Watters & Romani 2011; Takata et al. 2011; Kalapotharakos et al. 2014). Since the GeV emission from PSR J1119–6127 likely originates from the outer magnetosphere, the suppression of the GeV emission in the relaxation stage suggests that the 2016 magnetar-like outburst affected the structure of the global magnetosphere, and such an influence probably at most continued for about six months.

5. SUMMARY

In this study, we have performed a multi-wavelength study for PSR J1119–6127 after its 2016 magnetar-like outburst. We compared the X-ray and radio pulse profiles measured in 2016 August and December. We found that the X-ray and radio peaks were roughly aligned at different epochs. From the joint phase-resolved spectrum in different epochs, we found that the observed X-ray spectra of both on-pulse and off-pulse phases in 2016 August are well described by two blackbody components plus a power-law (a photon index $\Gamma = 0.5-1$) model. The power-law component did not show a significant modulation with the spin phase.

In gamma-ray bands, the GeV emission might be slightly suppressed around X-ray outburst. Based on the evolution of the GeV flux and of the spin-down rate, we divided the *Fermi* data into three epochs; pre-outburst epoch, outburst/relaxation epoch in 2016 July–2017 January and post-relaxation epoch after 2017 January. We found that the GeV spectral characteristics in the post-relaxation epoch are consistent with that of the pre-outburst epoch. Moreover, we confirmed the gamma-ray pulsation in post-relaxation epoch and the pulse shape is also consistent in terms of pulse profile with that of the pre-outburst stage. The phase difference between the gamma-ray peak and radio peak in post-relaxation stage is ~ 0.4 , which is consistent with the measurement before the X-ray outburst.

The radio/X-ray emission properties and the spin-down properties of PSR J1119–6127 after the X-ray outburst are similar to those of the magnetar XTE J1810–197. The similarities between two pulsars support the identification of the 2016 X-ray outburst of PSR J1119–6127 as magnetar-like activities. The 2016 X-ray outburst probably caused a re-configuration of the global magnetosphere and changed the structure of the open field line regions. The temporal evolution of the spin-down rate and the radio emission after the X-ray outburst will be related to the evolution of the structure of the open field line regions. The evolution of the X-ray emission will be related to the heating of the crust and/or stellar surface. We reproduce the evolution of the

observed X-ray flux with the untwisting magnetosphere model with particular model parameters (e.g., twist angle and potential drop). The multi-wavelength emission properties suggest that the reconfiguration of the global magnetosphere continued about a half-year after the X-ray outburst. The observed relation in the phase difference of the radio/gamma-ray peak positions before and after the X-ray outburst would suggest that the structure of magnetosphere has recovered to a normal state within ~ 0.6 years after the outburst.

We thank to referee for his/her useful comments and suggestions. We thank to M. Kerr for his useful discussion and suggestions. We also appreciate Drs Matthew Baring, D.J. Thompson and P. Bruel for their critical reading to polish our paper. In addition, we thank to N. K. Y. Low for his help to check the timing solution derived in the radio band. W.H.H. and J.T. are supported by the National Science Foundation of China (NSFC) under 11573010, 11661161010, U1631103 and U1838102. L.C.-C.L. and K.L.L. are supported by the National Research Foundation of Korea (NRFK) through grant 2016R1A5A1013277. C.-P.H. is supported by a GRF grant of the Hong Kong Government under HKU 17300215. X.H. is supported by the National Natural Science Foundation of China (NSFC-U1938103 and NSFC-11673060) and the Light of West China Program of the Chinese Academy of Sciences.

The *Fermi* LAT Collaboration acknowledges generous ongoing support from a number of agencies and institutes that have supported both the development and the operation of the LAT as well as scientific data analysis. These include the National Aeronautics and Space Administration and the Department of Energy in the United States, the Commissariat à l’Energie Atomique and the Centre National de la Recherche Scientifique / Institut National de Physique Nucléaire et de Physique des Particules in France, the Agenzia Spaziale Italiana and the Istituto Nazionale di Fisica Nucleare in Italy, the Ministry of Education, Culture, Sports, Science and Technology (MEXT), High Energy Accelerator Research Organization (KEK) and Japan Aerospace Exploration Agency (JAXA) in Japan, and the K. A. Wallenberg Foundation, the Swedish Research Council and the Swedish National Space Board in Sweden.

Additional support for science analysis during the operations phase is gratefully acknowledged from the Istituto Nazionale di Astrofisica in Italy and the Centre National d’Études Spatiales in France. This work performed in part under DOE Contract DE-AC02-76SF00515. This work made use of data supplied by the LAT data server of the Fermi Science Support Center (FSSC) and the archival data server of NASA’s High Energy Astrophysics Science Archive Research Center (HEASARC).

Facilities: *Parkes*, *Fermi*(LAT), *Swift*(XRT), *XMM*(EPIC), *NuSTAR*.

REFERENCES

- Abdo, A. A., Ajello, M., Allafort, A., Baldini, L., et al. 2013, *ApJS*, 208, 17
 Antonopoulou, D., Weltevrede, P., Espinoza, C. M., et al. 2015, *MNRAS*, 447, 3924
 Aliu, E., Anderhub, H., Antonelli, L. A., et al. 2008, *Science*, 322, 1221
 Archibald, R. F., Kaspi, V. M., Tendulkar, S. P., et al. 2016, *ApJ*, 829, L21
 Archibald, R. F., Burgay, M., Lyutikov, M., Kaspi, V. M., et al. 2017, *ApJL*, 849, L20
 Archibald, R. F., Kaspi, V. M., Tendulkar, S. P., et al. 2018, *ApJ*, 869, 180

- Arons, J. 1983, *ApJ*, 266, 215
- Atwood, W. B., Abdo, A. A., Ackermann, M., et al. 2009, *ApJ*, 697, 1071
- Atwood, W., Albert, A., Baldini, L., et al. 2013, arXiv e-prints, arXiv:1303.3514
- Beloborodov, A. M. 2009, *ApJ*, 703, 1044
- Blumer, H., Safi-Harb, S., & McLaughlin, M. A. 2017, *ApJ*, 850, L18
- Burgay, M., Possenti, A., Kerr, M., Esposito, P., et al. 2016, *The Astronomer's Telegram*, 9366
- Camilo, F., Kaspi, V. M., Lyne, A. G., et al. 2000, *ApJ*, 541, 367
- Camilo, F., Ransom, S. M., Halpern, J. P., Reynolds, J., Helfand, D. J., et al. 2006, *Nature*, 442, 892
- Caswell, J. L., McClure-Griffiths, N. M., & Cheung, M. C. M. 2004, *MNRAS*, 352, 1405
- Cheng, K. S., Ho, C., & Ruderman, M. 1986, *ApJ*, 300, 500
- Crawford, F., Gaensler, B. M., Kaspi, V. M., et al. 2001, *ApJ*, 554, 152
- Dai, S., Johnston, S., Weltevrede, P., et al. 2018, *Monthly Notices of the Royal Astronomical Society*, 480, 3584
- Dai, S., Johnston, S., Weltevrede, P., et al. 2019, *The Astrophysical Journal*, 874, L14
- De Jager, O., & Büsching, I. 2010, *Astronomy & Astrophysics*, 517, L9
- Dib, R., Kaspi, V. M., & Gavriil, F. P. 2008, *ApJ*, 673, 1044
- Enoto, T., Shibata, S., Kitaguchi, T., et al. 2017, *ApJS*, 231, 8
- Gonzalez, M., & Safi-Harb, S. 2003, *ApJ*, 591, L143
- Gotthelf, E. V., Halpern, J. P., Alford, J. A. J., et al. 2019, arXiv:1902.08358
- Gögüs, E., Lin, L., Kaneko, Y., et al. 2016, *ApJ*, 829, L25
- Hobbs G. B., Edwards R. T., Manchester R. N., 2006, *MNRAS*, 369, 655
- Hotan, A. W., van Straten, W., & Manchester, R. N. 2004, *Publications of Astronomical Society of Australia*, 21, 302
- Huang, L., Yu, C., & Tong, H. 2016, *The Astrophysical Journal*, 827, 80
- Ibrahim, A. I., Markwardt, C. B., Swank, J. H., et al. 2004, *ApJ*, 609, L21
- Johnston, S., & Weisberg, J. M. 2006, *MNRAS*, 368, 1856
- Kalopotharakos, C., Harding, A. K., & Kazanas, D. 2014, *ApJ*, 793, 97
- Kaspi, V. M., Gavriil, F. P., Woods, P. M., Jensen, J. B., Roberts, M. S. E., & Chakrabarty, D., et al. 2003, *ApJ*, 588, L93
- Kaspi, V. M., & Beloborodov, A. M. 2017, *ARA&A*, 55, 261
- Kennea, J. A., Lien, A. Y., Marshall, F. E., et al. 2016, *GRB Coordinates Network, Circular Service, No. 19735, #1* (2016), 19735
- Kerr, M. 2011, *ApJ*, 732, 38
- Lin, L. C.-C., Wang, H.-H., Li, K.-L., et al. 2018, *ApJ*, 866, 6
- Livingstone, M. A., Kaspi, V. M., & Gavriil, F. P. 2010, *ApJ*, 710, 1710
- Livingstone, M. A., Ransom, S. M., Camilo, F., et al. 2009, *ApJ*, 706, 1163
- Lyne, A., Levin, L., Stappers, B., et al. 2018, *The Astronomer's Telegram*, 12284
- Majid, W. A., Pearlman, A. B., Dobрева, T., et al. 2017, *ApJ*, 834, L2
- Manchester, R. N., Hobbs, G. B., Teoh, A., & Hobbs, M. 2005, *AJ*, 129, 1993
- Mihara, T., Negoro, H., Kawai, N., et al. 2018, *The Astronomer's Telegram*, 12291
- Morrison, R., & McCammon, D. 1983, *ApJ*, 270, 119
- Ng, C.-Y., Kaspi, V. M., Ho, W. C. G., et al. 2012, *ApJ*, 761, 65
- Ng, C.-Y., Kaspi, V. M., Dib, R., et al. 2011, *ApJ*, 729, 131
- Parent, D., Kerr, M., den Hartog, P. R., et al. 2011, *ApJ*, 743, 170
- Petroff, E., Keith, M. J., Johnston, S., et al. 2013, *MNRAS*, 435, 1610
- Pierbattista, M., Harding, A. K., Gonthier, P. L., Grenier, I. A. 2016, *A&A*, 588, A137
- Pons, J. A., & Rea, N. 2012, *The Astrophysical Journal Letters*, 750, L6
- Ray, P. S., Kerr, M., Parent, D., et al. 2011, *ApJS*, 194, 17
- Romani, R. W. 1996, *ApJ*, 470, 469
- Safi-Harb, S., & Kumar, H. S. 2008, *ApJ*, 684, 532
- Takata, J., Wang, Y., & Cheng, K. S. 2011, *MNRAS*, 415, 1827
- Takata, J., Cheng, K. S., & Taam, R. E. 2012, *ApJ*, 745, 100
- Takata, J., Ng, C. W., & Cheng, K. S. 2016, *MNRAS*, 455, 4249
- Thompson, C., & Duncan, R. C. 1996, *ApJ*, 473, 322
- Thompson, C., Duncan, R. C., Woods, P. M., et al. 2000, *ApJ*, 543, 340
- Watters, K. P., Romani, R. W., Weltevrede, P., et al. 2009, *ApJ*, 695, 1289
- Watters, K. P. & Romani, R. W. 2011, *ApJ*, 727, 123
- Weltevrede, P., Johnston, S., & Espinoza, C. M. 2011a, *MNRAS*, 411, 1917
- Weltevrede, P., Johnston, S., & Espinoza, C. M. 2011b, *MNRAS*, 411, 1917
- Weng, S.-S., Zhang, S.-N., Yi, S.-X., et al. 2015, *MNRAS*, 450, 2915
- Woods, P. M., & Thompson, C. 2006, *Soft gamma repeaters and anomalous X-ray pulsars: magnetar candidates*, ed. W. H. G. Lewin & M. van der Klis, 547–586
- Woods, P. M., Kaspi, V. M., Thompson, C., et al. 2004, *ApJ*, 605, 378
- Younes, G., Kouveliotou, C., & Roberts, O. 2016, *GRB Coordinates Network, Circular Service, No. 19736, #1* (2016), 19736